Research on Chemical Intermediates (2024) 50:817–838
https://doi.org/10.1007/s11164-023-05173-6

# Synthesis of 1, 8-dioxodecahydroacridines using core–shell structured $Fe_3O_4$@MgO MNP's: a solvent-free protocol

**Gayatree Shinde**[1,2] · **Jyotsna Thakur**[2]

Received: 13 September 2023 / Accepted: 29 October 2023 / Published online: 24 November 2023


## Abstract

This study presented a solvent-free synthesis of 1,8-dioxodecahydroacridine derivatives by a one-pot condensation reaction between cyclic 1,3-diketone, aldehydes using $Fe_3O_4$@MgO core–shell structured nanocatalyst up to 89–98% yield. The study was conducted using both the substrate—ammonium acetate and aniline. The nanocatalyst was synthesized by a simple co-precipitation method and found to be both facile and efficient in facilitating the synthesis of the desired derivatives in a short reaction time (5–18 min). The present methodology offers several advantages, such as low cost, magnetically recoverable and reusable catalyst, solvent-free strategy, easy setup, high yield, and short reaction time, clearly portraying the present reaction's green approach.

## Graphical abstract

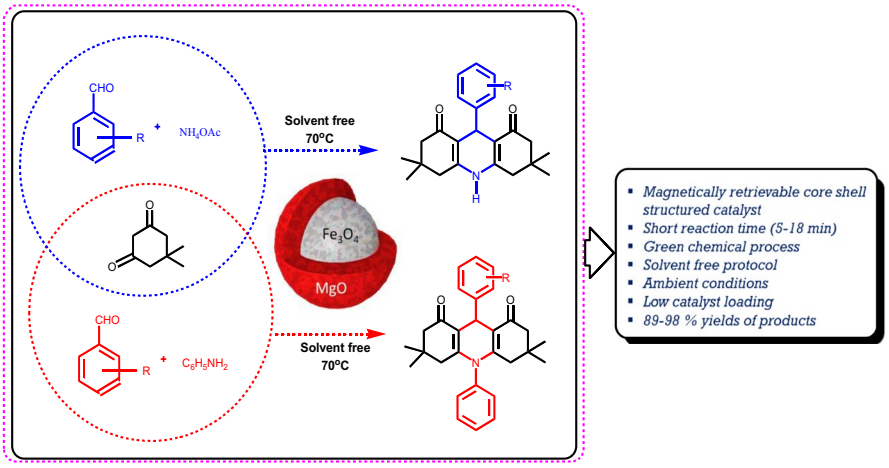


**Keywords** 1,8-dioxodecahydroacridine · $Fe_3O_4$@MgO · Core–shell nanocatalyst · Magnetically recoverable · Solvent-free

Extended author information available on the last page of the article

## Introduction

In synthetic organic and medicinal chemistry, the development of novel analogues of bioactive heterocyclic molecules is a significant challenge [1, 2]. In this context, N-containing heterocyclic compound derivatives possess favorable biological features, including antimalarial, antibacterial, anti-histaminic, anti-hypertensive, and anti-inflammatory activities [3–5].

Acridine derivatives exhibit various biological activities, including antibacterial, antimalarial, anticancer, and mutagenic properties [6, 7]. The pharmacological activity of acridine systems has garnered significant interest [8]. Acridine and its derivatives are widely used in industrial applications [9]. These compounds have been known since the nineteenth century and were initially utilized as pigments and dyes [10]. Thus far, various chemical and physical properties have been observed in acridine derivatives [11]. Their efficacy in the pharmaceutical sector has also been documented. The synthesis of acridine derivatives is a crucial and fundamental objective in organic chemistry [12]. There has been a notable emphasis on the fabrication of 1,8-dioxodecahydroacridines owing to their noteworthy physiological and biological functionalities, encompassing antimicrobial [13], anti-tumor [14], anti-inflammatory [15], cytotoxic [16], analgesic [17] and anti-fungal [18] attributes. The compounds under investigation are frequently synthesized via a tricomponent reaction, wherein 1,3-diketone, aldehydes, and a range of anilines or ammonium acetate are employed. The reaction under consideration is commonly catalyzed by a variety of catalysts, including Carbon-Based Solid Acid [19], PPA-$SiO_2$ [20], ammonium Chloride [21], polyvinylpolypyrrolidone-supported boron trifluoride [22], PPA/$Al_2O_3$ [23], Amberlite IR-120H [24], Cu(II) schiff Base [25], Cu-doped ZnO [26], 1,3-di (bromo or chloro)-5,5-dimethylhydantoin [27] and proline [28]. Nevertheless, it is essential to note that several methodologies previously reported in the literature present inherent constraints. These limitations encompass prolonged reaction times, the requirement for stoichiometric amounts of reagents, the necessity of expensive catalysts, the formation of low product yields, the utilization of toxic solvents, the implementation of conventional work-up protocols, difficulties in catalyst separation, and the inability to recover the catalyst [29, 30]. The discovery of novel methodologies utilizing new heterogeneous and reusable catalysts is still required to enhance the reaction conditions for the synthesis of 1,8-dioxodecahydroacridines and overcome the associated limitations [31].

In this regard, scientists have given considerable attention to magnetic nanostructures [32, 33]. They provide numerous size-related aspects, including a wide surface area, fine-tuning of the features, increased loading capacity, outstanding dispersion, remarkable stability, and simple catalyst reprocessing, enhancing heterogeneous catalysis's effectiveness in MCR [34]. Earlier studies have shown that incorporating magnetized nanomaterials with other potentially reactive components in core–shell nanostructures improves catalytic efficiency [35–39]. Due to their nanoscale size effect, well-controlled design, and modifiable

physicochemical characteristics, core–shell nanomaterials have attracted a great deal of interest, which has led to their applicability in a variety of popular research subjects [40, 41]

Magnetic nanocatalysts exhibit exceptional characteristics that render them highly advantageous for organic reactions [42–46]. The nanoscale dimensions of these particles result in a favorable surface area-to-volume ratio, which enhances their catalytic efficiency. Moreover, the inherent magnetic properties of these entities facilitate effortless extraction from reaction mixtures through the application of external magnetic fields, thereby promoting recyclability and minimizing waste generation. Moreover, the surface modifications and functionalizations of these catalysts can be customized, thereby augmenting their selectivity and reactivity towards particular organic transformations [47]. The aforementioned attributes, when coupled with their inherent stability and capacity for repeated utilization, render magnetic nanocatalysts exceptionally well-suited for a wide range of organic reactions. Consequently, their implementation plays a pivotal role in propelling the field of environmentally friendly and sustainable chemistry forward [48]. The core–shell structured nanocatalyst exhibits intriguing properties such as size-dependent characteristics, a core–shell structure, and magnetic behavior, rendering it a compelling option for catalyzing organic transformations [49].

The magnetic core of the catalyst is composed of $Fe_3O_4$ nanoparticles, which are encircled by a slender shell of MgO. The $Fe_3O_4$ core confers magnetic separability and significant support to the shell. Magnesium oxide, in its pure form, is a durable catalyst utilized in heterocyclic reactions [50].

Size-dependent characteristics, core–shell structure, and magnetic nature of $Fe_3O_4$@MgO make it an exciting choice as a catalyst in organic transformations [51–53]. $Fe_3O_4$ nanoparticles constitute the catalyst's magnetic core, which is surrounded by a thin MgO shell. The $Fe_3O_4$ core provides magnetic separability and substantial support to the shell. Pure MgO is a robust catalyst that is employed in heterocyclic processes. The significance of magnesium oxide (MgO) nanocatalysts in the realm of organic synthesis cannot be overstated [54, 55], owing to their remarkable catalytic efficiency, high stability, noteworthy adaptability, good surface characteristics, and substantial surface area, leaching resistance, low cost, redox properties, high dielectric constant. The combination of MgO and $Fe_3O_4$ offers numerous advantages in catalysis, which makes the approach easy, one-pot, inexpensive, and greener. These include simple preparation, high surface-to-volume ratio, wide availability, cost–benefit, environmental friendliness, easy recovery, and low catalyst loading.

The paper described the successful synthesis of magnetically separable core–shell structured $Fe_3O_4$@MgO nanocatalysts via a simple two-step co-precipitation process. These nanoparticles showed remarkable potential as a catalyst in the synthesis of 1,8-dioxodecahydroacridines under solvent-free conditions (Scheme 1).

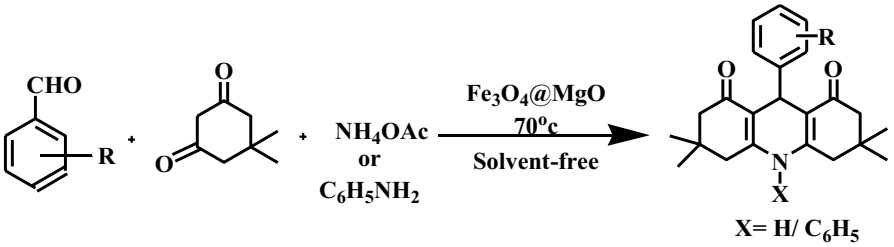


**Scheme 1** Synthesis of 1,8-dioxodecahydroacridines using $Fe_3O_4$@MgO nanocatalyst

## Experimental

### Synthesis of $Fe_3O_4$@MgO nanocatalyst

$Fe_3O_4$@MgO was synthesized in two steps as follows-

#### Step I: synthesis of $Fe_3O_4$ nanoparticles

$Fe_3O_4$ nanoparticles were synthesized by slight modification in the previously reported co-precipitation method [56] by mixing stoichiometric amounts of 0.2 M $FeCl_3.6H_2O$ (50 mL, 1.62 g) and 0.1 M $FeCl_2.4H_2O$ (50 mL, 0.80 g). The resulting mixture was sonicated for 30 min, followed by mechanical stirring at 80 °C for 1 h till a transparent solution appeared. The pH of the solution was adjusted to alkaline pH by adding 25% ammonium hydroxide gradually. The precipitate formed was allowed to settle and then isolated from the liquid phase by applying an external magnet. The precipitate was rinsed multiple times using distilled water until a neutral pH was achieved. The resulting black precipitate was dried for 6 h at 60 °C (Fig. 1). The following reaction can describe the potential chemical transformation within this experimental procedure:

$$2FeCl_3 + FeCl_2 + 8NH_4OH \rightarrow Fe_3O_4 + 8NH_4Cl + 4H_2O$$

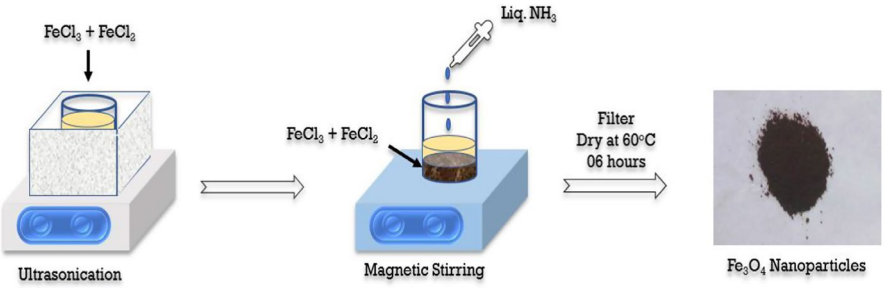


**Fig. 1** Synthesis of $Fe_3O_4$ nanocatalyst

### Step II: synthesis of $Fe_3O_4$@MgO by surface modification

Coating of MgO on $Fe_3O_4$ nanoparticles was carried out by the method described by Peng et al. [52]. 0.5 g of as-prepared $Fe_3O_4$ nanoparticles were dispersed in 100 mL of CTAB (1 g) solution, used as a stabilizing and capping agent [57], and sonicated for 30 min. 50 mL of a 0.5 mol $L^{-1}$ $MgCl_2$ solution was added to the mixture and stirred for 1 h at room temperature. Further, the temperature was raised to 70 °C, and ammonia solution was added with constant stirring for 4 h. The mixture was allowed to cool to room temperature. The resulting product was washed multiple times with ethanol before being dried for 6 h at 50 °C. The product was calcined at different temperatures, such as 450 °C, 550 °C, and 650 °C, for 3 h. This resulted in a brown-colored powder of $Fe_3O_4$@MgO (Fig. 2).

The synthesized catalyst is characterized by using various techniques. The Powder X-ray diffraction (PXRD) was recorded using a Bruker D8 Advance Twin-Twin instrument. JEOL JSM-7600F FEG-SEM, in conjunction with energy dispersive spectroscopy (EDS) and element mapping with an EDS analyzer, were used for the analysis of surface morphology. The shape and size of the nanocomposite were investigated using a high-resolution transmission electron microscope; Tecnai G2, F30 HRTEM-200 kV. The Magnetic properties were measured using Lakeshore VSM 7410S series. Micromeritics, ASAP 2010 was used to analyzed the BET surface area of nanocatalyst. The zeta potential/surface charge of the nanocatalyst was determined using Zetasizer 3000, Malvern Instruments. The particle size of the nanocatalyst was determined using HORIBA SZ-100 instrument.

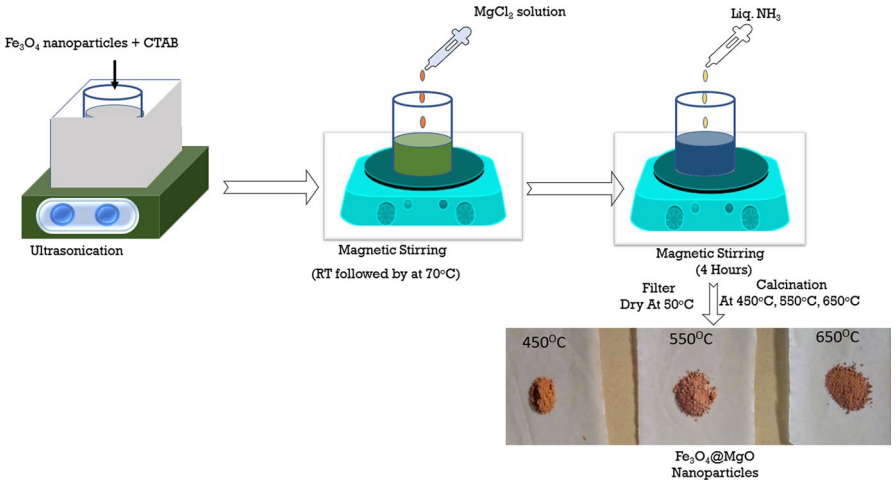


**Fig. 2** Synthesis of $Fe_3O_4$@MgO nanocatalyst

### Synthesis of 3,3,6,6-tetramethyl-9-aryl-3,4,6,7,9,10-hexahydro-2H,5H-acridine-1,8-dione

A mixture of aromatic aldehyde (1 mmol), dimedone (2 mmol), and ammonium acetate/ aniline (1 mmol) is heated in the presence of a catalytic amount of $Fe_3O_4$@ MgO (15 mg) under solvent-free conditions at 70 °C for the stipulated time. The progress of the reaction was monitored by TLC (n-Hexane: EtOAc, 9:1). The final product was heated in ethanol and poured into water. The catalyst was magnetically removed and washed with chloroform for reuse. The residue was then poured into crushed ice and stirred. The pure product was obtained by recrystallization from hot aqueous alcohol. This resulted in the production of 3,3,6,6-tetramethyl-9-phenyl-3,4,6,7,9,10-hexahydro-2H,5H-acridine-1,8-dione with a yield of 89–98% (Table 1, Entry 1–13).

The synthesized compounds' melting points were determined using the open capillary method and reported without additional adjustments. The presence of specific functional groups in the molecule was determined by recording the Fourier Transform Infrared (FT-IR) spectrum of the products using a Vertex 80 FTIR System (Bruker, Germany) with a 3000 Hyperion Microscope. Proton nuclear magnetic resonance ($^1$H NMR) spectroscopy and 13C nuclear magnetic resonance spectroscopy were carried out in DMSO using tetramethylsilane (TMS) as an internal standard on a 400 MHz and 100 MHz liquid-state nuclear magnetic resonance (NMR) spectrometer instrument respectively. The chemical shifts (δ) of all Proton atoms

**Table 1** Synthesis of 1,8-dioxo-9-aryl decahydroacridine and 1,8-dioxo-9,10-diaryl decahydroacridine derivatives[a]

| Entry | Aldehyde | $NH_4OAc$/Aniline | Time (Min) | Yield [b] (%) | M.P (ºC) | Lit M.P (ºC) |
|---|---|---|---|---|---|---|
| 1 | Benzaldehyde | $NH_4OAc$ | 11 | 95 | 246–248 | 249–251 [58] |
| 2 | 4-Nitro benzaldehyde | $NH_4OAc$ | 09 | 97 | 287–289 | 284–287 [58] |
| 3 | 4-Hydroxy benzaldehyde | $NH_4OAc$ | 14 | 94 | 290–292 | > 300 [59] |
| 4 | 4- (N, N-Dimethyl) amino benzaldehyde | $NH_4OAc$ | 14 | 95 | 284–286 | 281–283 [58] |
| 5 | 2-Hydroxy benzaldehyde | $NH_4OAc$ | 13 | 91 | 270–274 | 271–273 [60] |
| 6 | Indol-3-carbaldehyde | $NH_4OAc$ | 15 | 89 | 274–276 | – |
| 7 | 4-Methyl benzaldehyde | $NH_4OAc$ | 12 | 92 | 298–299 | > 300 [59] |
| 8 | 2-Chloro benzaldehyde | $NH_4OAc$ | 10 | 90 | 294–297 | 298–301 [58] |
| 9 | 4-Bromo benzaldehyde | $NH_4OAc$ | 18 | 96 | 240–242 | 236–238 [59] |
| 10 | 4-Methoxy benzaldehyde | $NH_4OAc$ | 14 | 92 | 267–269 | 271–272 [58] |
| 11 | Benzaldehyde | Aniline | 6 | 98 | 254–255 | 253–255 [59] |
| 12 | 4-Nitro benzaldehyde | Aniline | 5 | 94 | 288–289 | 281–282 [61] |
| 13 | 4-Methoxy benzaldehyde | Aniline | 12 | 95 | 222–223 | 219–223 [59] |

[a]Reaction conditions: aldehyde (1 mmol), dimedone (2 mmol), ammonium acetate/aniline (1 mmol), and 15 mg of $Fe_3O_4$@MgO at 70 °C under solvent-free conditions

[b]Yield of isolated products

are determined relative to tetramethyl silane (TMS, δ = 0.00) as an internal standard. Additionally, coupling constants (*J*) are expressed in units of Hz.

### Spectral data of representative organic molecules

**3,3,6,6-Tetramethyl-9-(4-nitro-phenyl)-3,4,6,7,9,10-hexahydro-2H,5H-acridine-1,8-dione** Table 1**, Entry 2:** Yellow solid**;** mp: 287–289 °C (EtOH); IR (KBr) υ $cm^{-1}$: 3215, 2957, 1730 1590, 1486, 1339, 1219, 832, 751; $^1$H NMR Spectrum (400 MHz, DMSO-$d_6$) δ, ppm (*J*, Hz): 8.44 (s, 1H), 7.95 (d, *J* = 7.4, 2H), 7.50 (d, *J* = 7.4, 2H), 4.45 (s, 1H), 2.43 (s, 4H), 1.68 (s, 4H), 1.09 (s, 12H); $^{13}$C NMR Spectrum (100 MHz, DMSO-$d_6$) δ, ppm:199.48, 194.51, 165.01, 159.55, 149.32, 145.68, 134.28, 128.99, 123.19, 112.54, 65.31, 51.49, 36.36, 32.86, 32.71, 28.81; Elemental analysis: Found %: C 70.09; H 6.68; N 7.02. $C_{23}H_{26}N_2O_4$. Calculated %: C 70.03; H 6.64; N 7.10.

**9-(4-Hydroxy-phenyl)-3,3,6,6-tetramethyl-3,4,6,7,9,10-hexahydro-2H,5H-acridine-1,8-dione** Table 1**, Entry 3:** White solid; mp**:** 290–292 °C (EtOH); IR (KBr) υ $cm^{-1}$: 3166, 2955, 2870, 1714, 1577, 1507, 1467, 1368, 1219, 1036, 833, 749; $^1$H NMR Spectrum (400 MHz, DMSO-$d_6$) δ, ppm (*J*, Hz): 9.08 (s, 1H), 8.27 (s, 1H), 7.16 (d, *J* = 7.4 Hz, 2H), 6.71 (d, *J* = 7.6 Hz, 2H), 4.42 (s, 1H), 2.05 (s, 4H), 1.61 (s, 4H), 1.11 (s, 12H); $^{13}$C NMR Spectrum (100 MHz, DMSO-$d_6$) δ, ppm: 194.68, 185.05, 159.64, 157.19, 129.32, 129.21, 115.15, 113.54, 91.34, 53.49, 36.40, 32.99, 32.62, 27.90; Elemental analysis: Found %: C 75.55; H 7.39; N 3.78. $C_{23}H_{27}NO_3$. Calculated %: C 75.59; H 7.45; N 3.83.

**9-(4-Dimethylamino-phenyl)-3,3,6,6-tetramethyl-3,4,6,7,9,10-hexahydro-2H,5H-acridine-1,8-dione** Table 1**, Entry 4:** Off-white solid; mp**:** 284–286 °C (EtOH); IR (KBr) υ $cm^{-1}$: 3736, 2873, 1740, 1581, 1366, 1237, 1063, 907, 809; $^1$H NMR Spectrum (400 MHz, DMSO-$d_6$) δ, ppm (*J*, Hz): 8.42 (s, 1H), 7.22 (d, *J* = 47.6 Hz, 2H), 6.93–6.43 (m, 2H), 5.51 (s, 6H), 5.43 (s, 1H), 2.41 (s, 4H), 2.11 (s, 4H), 1.33–0.90 (m, 12H); $^{13}$C NMR Spectrum (100 MHz, DMSO-$d_6$) δ, ppm: 190.26, 189.28, 148.77, 127.49, 125.61, 115.97, 112.69, 47.09, 46.50, 40.72, 31.84, 31.38, 29.72, 27.35; Elemental analysis: Found %: C 76.09; H 8.20; N 7.11. $C_{25}H_{32}N_2O_2$. Calculated %: C 76.49; H 8.22; N 7.14.

**9-(2-Hydroxy-phenyl)-3,3,6,6-tetramethyl-3,4,6,7,9,10-hexahydro-2H,5H-acridine-1,8-dione** Table 1**, Entry 5:** White solid; mp**:** 270–274 °C (EtOH); IR (KBr) υ $cm^{-1}$: 3300, 3123, 2957, 1714, 1584, 1450, 1368, 1219, 1145, 829, 738; $^1$H NMR Spectrum (400 MHz, DMSO-$d_6$) δ, ppm (*J*, Hz): 9.11 (s, 1H) 8.15 (s, 1H), 7.14–6.98 (m, 2H), 6.81–6.30 (m, 2H), 4.45 (s, 1H), 2.06 (s, 4H), 1.61 (s, 4H), 1.11 (s, 12H); $^{13}$C NMR Spectrum (100 MHz, DMSO-$d_6$) δ, ppm: 203.54, 196.52, 166.27, 136.43, 133.83, 126.22, 122.68, 121.16, 119.56, 118.57, 110.93, 53.98, 51.77, 46.72, 32.38, 28.25; Elemental analysis: Found %: C 75.50; H 7.34; N 3.81. $C_{23}H_{27}NO_3$ Calculated %: C 75.59; H 7.45; N 3.83.

**9-(1H-Indol-3-yl)-3,3,6,6-tetramethyl-3,4,6,7,9,10-hexahydro-2H,5H-acridine-1,8-dione** Table 1**, Entry 6:** Yellow crystals; mp**:** 274–276 °C (EtOH); IR (KBr) υ $cm^{-1}$: 3738, 2957, 1707, 1583, 1366, 1255, 1148, 927, 748, 664; $^1$H NMR Spectrum (400 MHz, DMSO-$d_6$) δ, ppm (*J*, Hz): 8.42 (s, 1H), 7.22 (d, *J* = 47.6 Hz, 1H), 6.93–6.43 (m, 5H), 5.51 (s, 1H), 2.41 (s, 4H), 2.11 (s, 4H),

1.33–0.90 (m, 12H); $^{13}$C NMR Spectrum (100 MHz, DMSO-$d_6$) δ, ppm: 192.93, 158.33, 138.62, 126.94, 123.52, 121.47, 121.45, 118.20, 114.61, 113.37, 108.13, 60.06, 51.49, 38.45, 36.36, 32.71, 28.81; Elemental analysis: Found %: C 77.13; H 7.22; N 7.08. $C_{25}H_{28}N_2O_2$ Calculated %: C 77.29; H 7.26; N 7.21.

## Result and discussion

### Characterization of the core–shell structured $Fe_3O_4$@MgO nanocatalyst

The XRD analysis of $Fe_3O_4$@MgO powder exhibited the characteristic peaks of the crystalline phase of $Fe_3O_4$ with MgO. X-ray diffraction (XRD) patterns of the $Fe_3O_4$, as well as $Fe_3O_4$@MgO (annealed at 450 °C), are shown in Fig. 3. The peaks observed at 38.04, 42.94, 62.40, 74.71 and 78.62 correspond to (111), (200), (220), (311), and (222) planes (JCPDS No. 87-0653), indicating the formation of polycrystalline cubic structure of $Fe_3O_4$@MgO nanoparticles. The intensity of diffraction peaks was increased with increasing the annealing temperature while the $Fe_3O_4$@MgO NPs were increased. It is observed that, as the annealing temperature is increased, the intensity of diffraction peaks increases. This may suggest that a high annealing temperature gives sufficient energy to crystallize in the proper orientation and produces a rise in intensity. [62].

The average crystallite size is determined by the Debye Scherrer formula based on the peak's full width at half-maximum (FWHM). It was observed that the rise in annealing temperature improves the crystallinity of the nanoparticles and, therefore, the crystallite size of $Fe_3O_4$@MgO nanoparticles (Table 2).

The HRTEM images (Fig. 4a, b) reveal the spherical-shaped core–shell particles of $Fe_3O_4$@MgO. The clear lattice fringes confirm the crystalline nature of

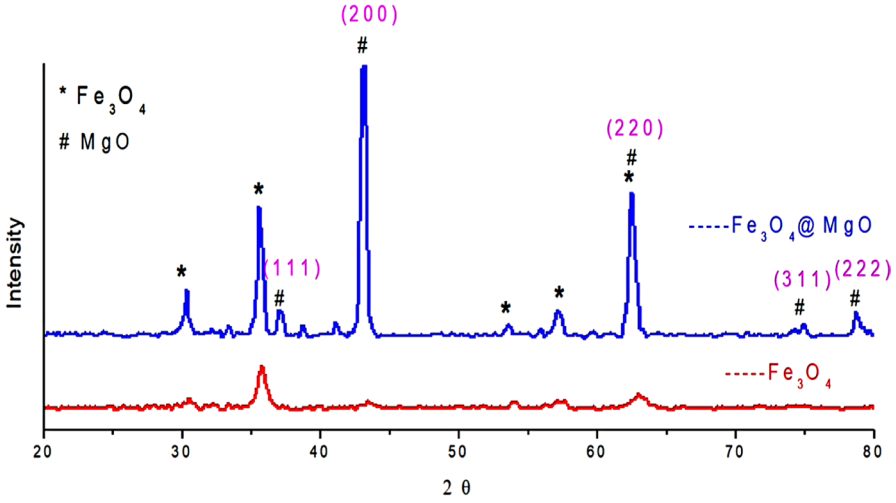


**Fig. 3** XRD pattern of $Fe_3O_4$ and $Fe_3O_4$@MgO calcined at 450 °C

**Table 2** Full Width at Half Maxima (FWHM) and average particle size of $Fe_3O_4$@MgO NP's at annealing temperatures of 450 °C, 550 °C, and 650 °C

| Nanoparticle | Annellation temp | FWHM of high-intensity peak | Average particle size |
|---|---|---|---|
| $Fe_3O_4$@MgO | **450** °C | **0.3225** | **27.69 ± 2.00** |
| | 550 °C | 0.2487 | 35.91 ± 1.5 |
| | 650 °C | 0.2122 | 42.09 ± 2.4 |

The bold signifies best-obtained crystallite size to show the suitable temperature condition

the $Fe_3O_4$ core. Some crystal planes are visible in the core structure calculated using ImageJ software. The Interlayer d-spacing was measured with ImageJ software, as illustrated in Fig. 4b. The d-spacing values of $Fe_3O_4$@MgO were calculated as 2.06, 2.12 Aº assigned to the (200) plane of MgO and 2.53, 2.49 Aº assigned to the (311) plane of $Fe_3O_4$ are in agreement with XRD results [53]. The selected area electron diffraction (SAED) pattern specifies the presence of polycrystalline crystal structures in the synthesized nanocatalyst (Fig. 4c).

SEM images showed that the $Fe_3O_4$@MgO nanoparticles are of a spherical morphology due to agglomeration of the nanoparticles (Fig. 5a). The formation of core–shell nanoparticles was confirmed from the elemental X-ray mapping in addition to HRTEM images (Fig. 5b).

EDAX analysis provides elemental composition/distribution (Fig. 5c). The nanocatalyst contains elemental magnesium, oxygen, and iron, as seen by the prominent peaks at 1.3, 0.6, and 6.5 keV. Fe, O, and Mg were 9.86%, 42.92%, and 47.21% by weight.

The magnetic characteristics of $Fe_3O_4$ and $Fe_3O_4$@MgO were analyzed using a vibrating sample magnetometer (VSM), as illustrated in Fig. 6. The magnetic properties of uncoated and MgO-coated $Fe_3O_4$ nanoparticles were analyzed by measuring the VSM graph. The measurements were done at room temperature using a magnetic field ranging from −15 to 15 kOe. The comparable values of coercivity and remanence suggest the persistence of superparamagnetic properties in $Fe_3O_4$ nanoparticles after forming their shell.

According to the magnetization curve, the $Fe_3O_4$ and $Fe_3O_4$@MgO samples exhibited saturation magnetization values of 58.76 and 5.76 emu $g^{-1}$, respectively. The drop in saturated magnetization observed in $Fe_3O_4$@MgO may be attributed to a magnetically inactive MgO layer in the prepared catalyst [51].

The simple and effective recovery of the catalyst is illustrated in Fig. 7. By applying an external magnet.

The surface area analysis using the Brunauer–Emmett–Teller (BET) method and results are presented in Table 3. The values showed that the nanocatalyst has a surface area of 31.1327 $m^2/g$. The BET isotherm linear plot showing the nitrogen adsorption–desorption cycle is presented in Fig. 8, which shows TYPE-IV isotherm [63], characteristic for mesoporous materials confirmed by the average pore diameter shown in Table 3.

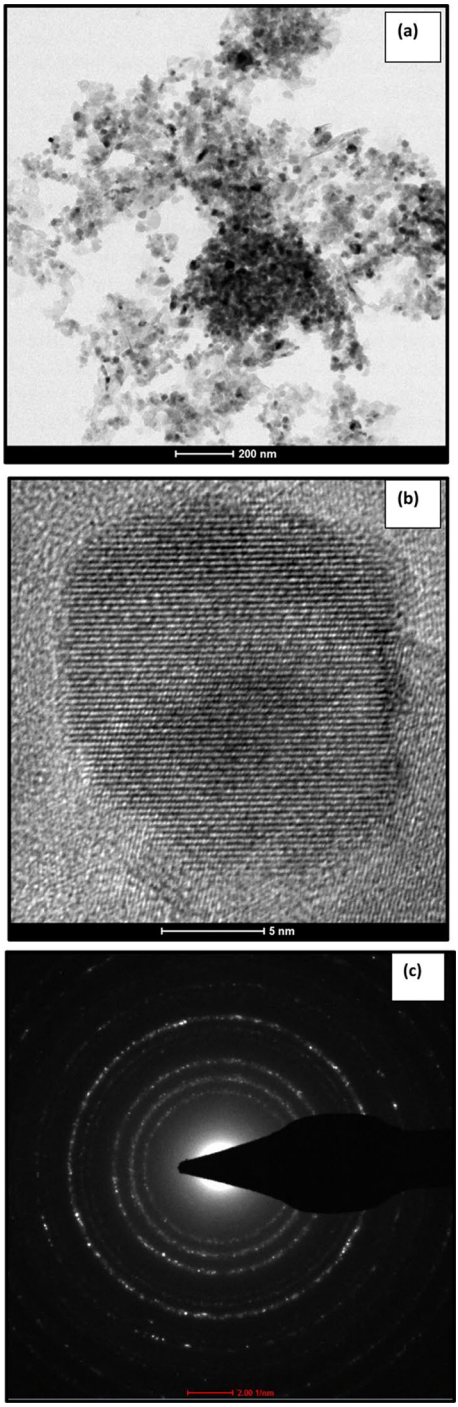


**Fig. 4** **a** TEM image; **b** High-resolution TEM image; **c** SAED pattern

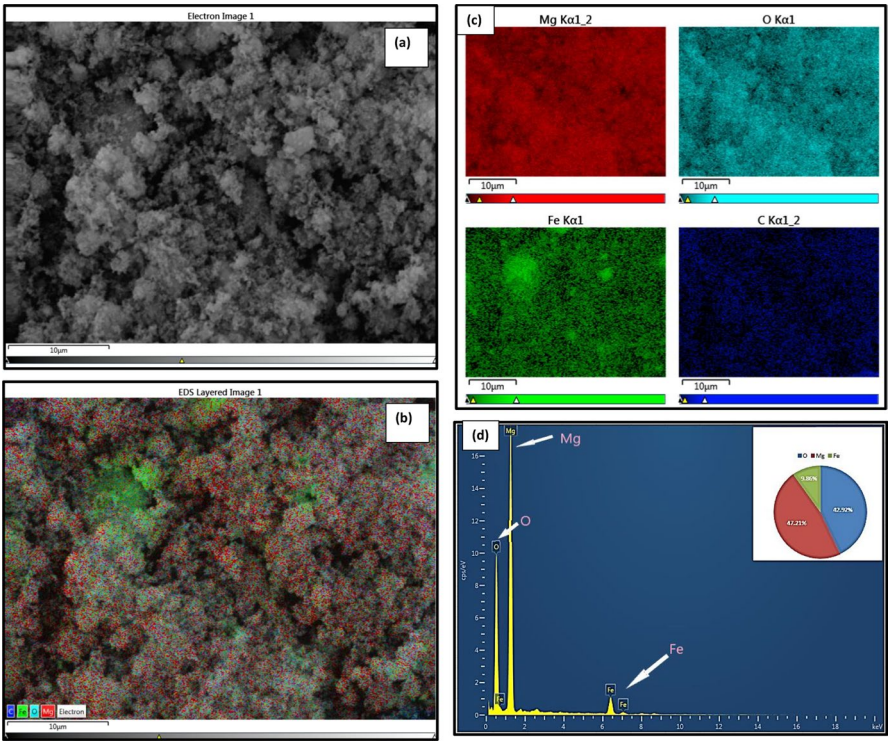


**Fig. 5** **a** SEM. **b** Surface mapping (Mixed image). **c** Mapped elements Mg, O, Fe, C. **d** EDX of $Fe_3O_4$@MgO core–shell nanoparticles

The Zeta potential value of nanocatalyst was + 44.16 mV, which suggests that the nanocatalysts exhibit colloidal stability and can be employed in heterogeneous catalytic reactions. The mobility distribution graph is shown in the Fig. 9

The Particle size of the $Fe_3O_4$@MgO nanocatalyst is found to be 27.60 nm, as shown in Fig. 10, which is in agreement with the XRD analysis.

## Study of catalytic efficiency of $Fe_3O_4$@MgO nanocatalyst for the synthesis of 1,8-dioxodecahydroacridine

This study presents a novel, simple, gentle, and effective approach for the one-step production of 1,8-dioxodecahydroacridine compounds using $Fe_3O_4$@MgO as a reusable catalyst. This catalyst exhibits environmentally sustainable properties, is easy to handle, and is quickly recoverable from the reaction mixture. The initial experiments demonstrated that the reaction of benzaldehyde (1 mmol), dimedone (2 mmol), and ammonium acetate (1 mmol) in a catalytic amount of $Fe_3O_4$@MgO (15 mg) under solvent-free conditions at 70 °C for 11 min resulted in the production of 3,3,6,6-tetramethyl-9-phenyl-3,4,6,7,9,10-hexahydro-2H,5H-acridine-1,8-dione with a yield of 95%.

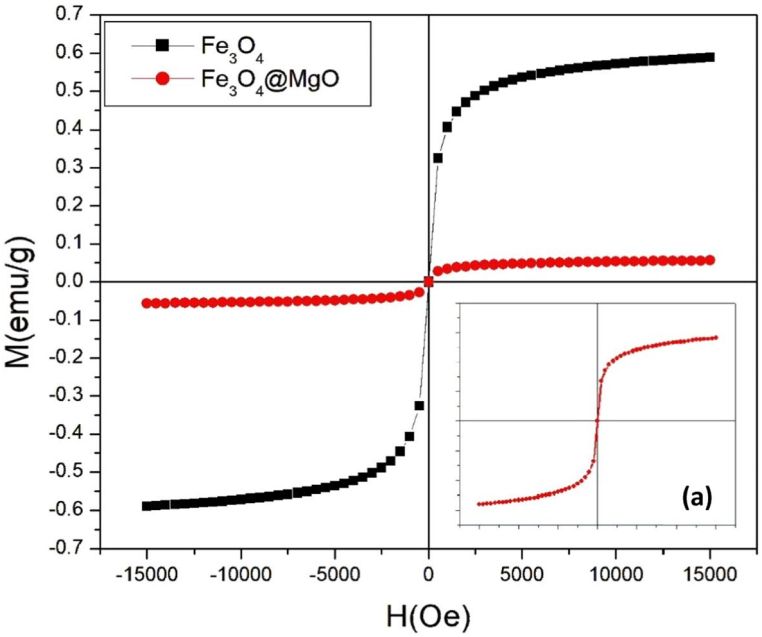


**Fig. 6** Magnetic study of the $Fe_3O_4$ and $Fe_3O_4$@MgO nanocatalyst (inset (**a**) enlarged VSM graph of $Fe_3O_4$@MgO)

**Fig. 7** Magnetic recovery of the catalyst from the reaction mixture

**Table 3** BET surface area, pore volume, and pore diameter of synthesized $Fe_3O_4$@MgO nanocatalyst

| Sample | BET surface area ($m^2\ g^{-1}$) | Average pore volume ($cm^3\ g^{-1}$) | Average pore diameter (nm) |
|---|---|---|---|
| $Fe_3O_4$@MgO | 31.1327 | 0.2141 | 26.38 |

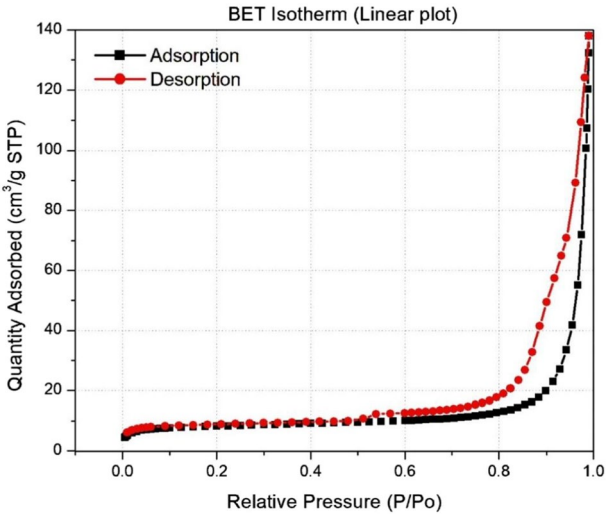


**Fig. 8** Adsorption desorption isotherm of the nanocatalyst

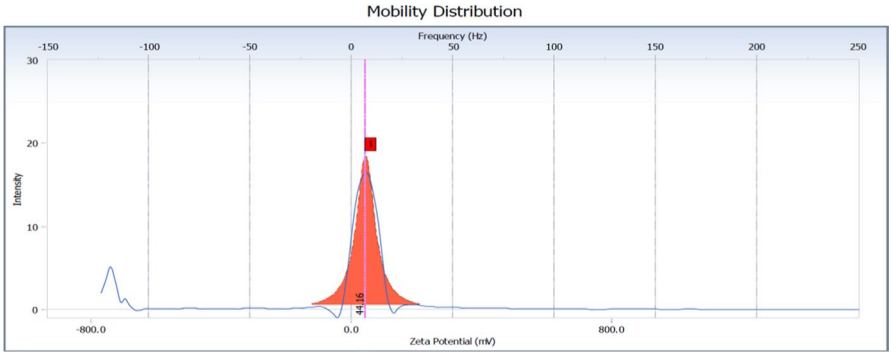


**Fig. 9** Mobility distribution plot

The synthesis of 1,8-dioxodecahydroacridine derivatives was achieved by reacting benzaldehyde, dimedone, and ammonium acetate in the presence of different solvents, as indicated in Table 4 (Entry 1–9). Additional reactions were conducted with various nitrogen sources, including ammonia and ammonium chloride, to assess their effectiveness in the proposed protocol (Table 4, Entry 10, 11). The results indicated that when ammonia or ammonium chloride was used instead of ammonium acetate, the product yield was significantly lower under the optimized reaction conditions. This could be attributed to the volatile nature of ammonia and ammonium acetate.

Figure 11 shows the assessment of catalytic loading, indicating that the most favorable output was achieved by utilizing a nanocatalyst of $Fe_3O_4$@MgO (15 mg)

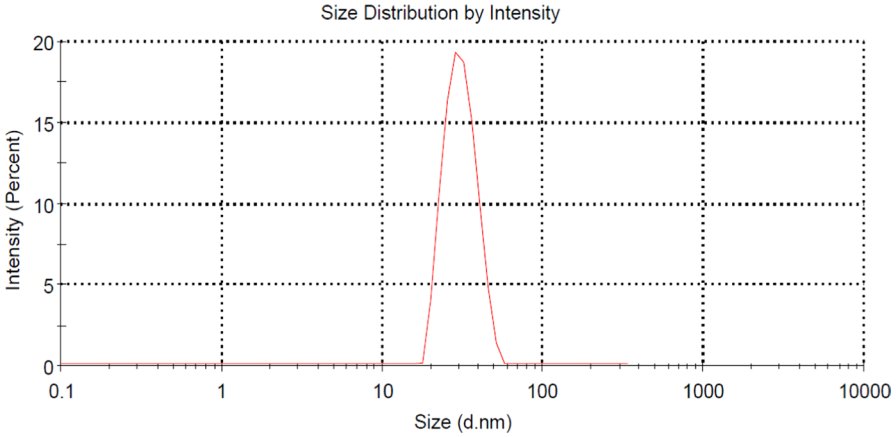


**Fig. 10** Particle size distribution plot

**Table 4** Optimization of reaction parameters for 3,3,6,6-tetramethyl-9-aryl-3,4,6,7,9,10-hexahydro-2H,5H-acridine-1,8-dione derivative synthesis by using $Fe_3O_4$@MgO catalysta (Table 1, Entry 1)

| Sr. no | Solvent/Temperature | Time (Min) | Yield[b] (%) |
|---|---|---|---|
| 1 | THF/Reflux | 42 | 75 |
| 2 | DMSO/Reflux | 48 | 71 |
| 3 | Ethylene glycol/Reflux | 45 | 68 |
| 4 | Ethanol/ Reflux | 25 | 79 |
| 5 | $H_2O$/ Reflux | 54 | 38 |
| 6 | Solvent-free/Reflux | 11 | 95 |
| **7** | **Solvent free/70 °C** | **11** | **95** |
| 8 | Solvent free/50 °C | 20 | 89 |
| 9 | Solvent-free/Room temp | 55 | 35 |
| 10 | Solvent free/70 °C | 41* | 34* |
| 11 | Solvent free/70 °C | 48** | 30** |

[a]Reaction conditions: benzaldehyde (1 mmol), dimedone (2 mmol), ammonium acetate (1 mmol), and 15 mg of $Fe_3O_4$@MgO; * benzaldehyde (1 mmol), dimedone (2 mmol), ammonia (1 mmol), and 15 mg of $Fe_3O_4$@MgO; ** benzaldehyde (1 mmol), dimedone (2 mmol), ammonium chloride (1 mmol), and 15 mg of $Fe_3O_4$@MgO

[b]Yield of isolated products

The bold signifies reaction protocol's significance and illustrate ideal reaction conditions

under solvent-free conditions at a temperature of 70 °C for the model reaction (refer to Fig. 11).

After establishing the reaction parameters, the applicability of the present protocol was demonstrated for aldehydes with a variety of functionalities and different sources of N (ammonium acetate and aniline). The resultant products were organized in tabular format systematically (Table 1). The reaction exhibited a high degree

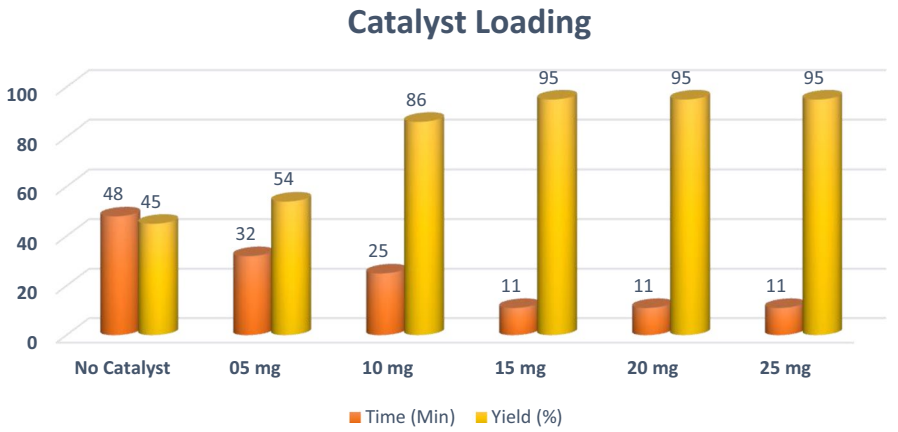


**Fig. 11** Study of catalyst loading in the model reaction (Table 1, Entry 1)

of selectivity, as evidenced by the absence of any detectable by-products in TLC screening. Furthermore, under the given reaction conditions, aniline exhibited a higher reaction rate as well as a high yield. This observation revealed that aniline is superior to ammonium acetate as a nitrogen source, which may attribute to the dual functionality of aniline, which acted as both a nucleophile and a hydrogen donor. The nucleophilic character of aniline facilitated its interaction with the carbonyl part of the substrate, resulting in the generation of the desired intermediate. Furthermore, the hydrogen donor property of aniline enabled the proton transfer mechanism, leading to the synthesis of the 1,8-dioxo decahydroacridine product. The synthesized decahydroacridine-1,8-diones were characterized through spectral studies.

Environmental compatibility of the existing synthetic protocol was assessed by applying established 'green chemistry metrics' such as E-factor, atom economy, reaction mass efficiency, optimum efficiency, and reaction mass yield, represented in Fig. 12. The E-factor ranging from 0.14 to 0.44 characterizes the environmental compatibility of reaction methodology. The other factors, like atom economy (75.39–89.70%), reaction mass efficiency (69.06–87.12%), and optimum efficiency (89–98%), are closely aligned to their respective benchmarks.

## Reusability study

The $Fe_3O_4$@MgO nanocatalyst exhibits magnetic recoverability without any significant loss. In order to assess the stability of the catalytic activity and the feasibility of recycling, a series of catalytic cycles were conducted. After each cycle, $Fe_3O_4$@MgO was washed using chloroform and was subsequently subjected to vacuum drying to eliminate any remaining solvent. The catalyst exhibited reusability for up to five cycles with negligible activity loss, as shown in Fig. 13. Following each trial, the X-ray diffraction (XRD) pattern of the utilized $Fe_3O_4$@MgO was found to be indistinguishable from that of the original $Fe_3O_4$@MgO,

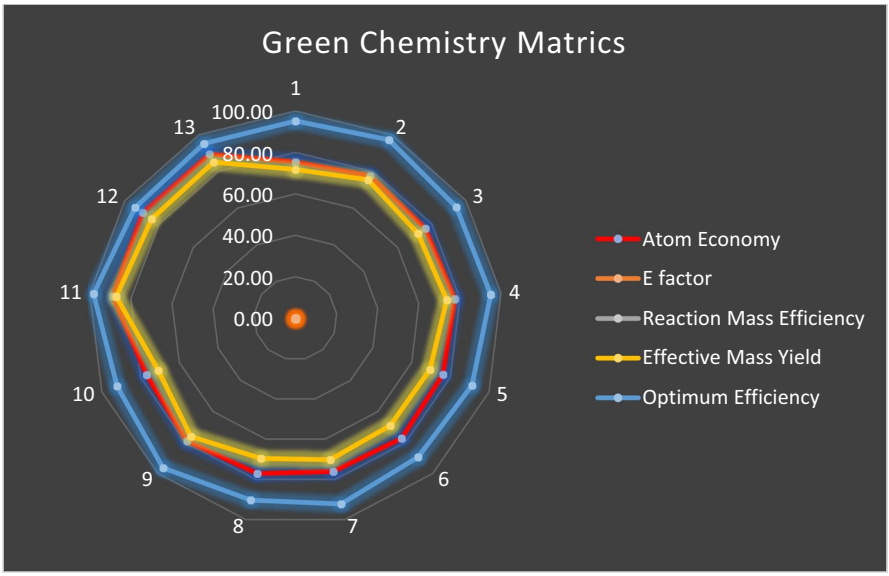


**Fig. 12** Radar chart for the calculated green matrices for the synthesis of 1,8-dioxodecahydroacridines

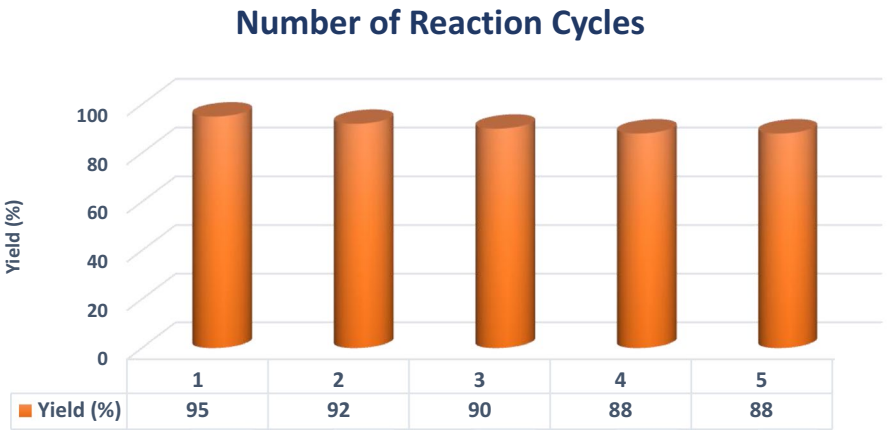


**Fig. 13** Reusability of the catalyst in the model reaction (Table 1, Entry 1)

indicating that the catalyst's framework structure remained intact during the reaction progression (as shown in Fig. 14). As a result, the catalyst appears to be reusable.

Furthermore, the proposed mechanism of the reaction elucidates the advancement of the multicomponent reaction. Based on our empirical research and other comparable findings, Fig. 15 illustrates a conceivable process for the production of decahydroacridine-1, 8-diones utilizing $Fe_3O_4$@MgO. At the outset, the catalytic sites that

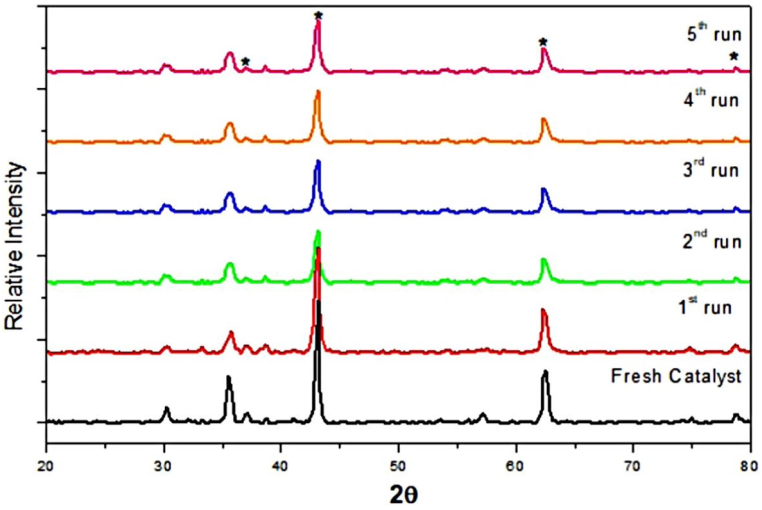


**Fig. 14** XRD studies of fresh and used catalysts in each run of the model reaction (Table 1, Entry 1)

are active augment the electrophilicity of aldehyde carbonyl groups while also facilitating the enolization of dimedone. After activating the aldehyde, the Knoevenagel product was obtained through a nucleophilic attack of dimedone. Following that, the Knoevenagel product undergoes a Michael-type reaction with a second molecule of dimedone, forming an intermediate compound. Subsequently, the obtained intermediate was reacted to an amine molecule, which undergoes intramolecular cyclization through dehydration, resulting in the formation of the final product [29].

## Comparative study of the catalyst

The current investigation explores the catalytic performance of $Fe_3O_4$@MgO with magnetic properties in the production of a 3,3,6,6-tetramethyl-9-aryl-3,4,6,7,9,10-hexahydro-2H,5H-acridine-1,8-dione derivative. The comparative analysis of the nanocatalyst's performance was conducted concerning the catalysts reported earlier. The findings of this investigation offer conclusive proof that the nanocrystalline magnetic $Fe_3O_4$@MgO catalyst is a viable, efficient, and cost-effective alternative for synthesizing 3,3,6,6-tetramethyl-9-aryl-3,4,6,7,9,10-hexahydro-2H,5H-acridine-1,8-dione derivative with a high yield rate under ambient reaction conditions. The findings delineated in Tables 5 and 6 demonstrate that the $Fe_3O_4$@MgO nanocatalyst is an exceptionally potent and proficient catalyst for the synthesis of 3,3,6,6-tetramethyl-9-aryl-3,4,6,7,9,10-hexahydro-2H,5H-acridine-1,8-dione derivative without the use of any solvents at 70 °C. The catalyst outperforms the efficacy of previously documented catalysts. A high product yield is achieved as a consequence of rapid chemical reactions. The magnesium oxide (MgO) displays a low specific weight, high melting point, and minimal lattice mismatch with magnetite. These characteristics make it a highly favorable substance for shell structure.

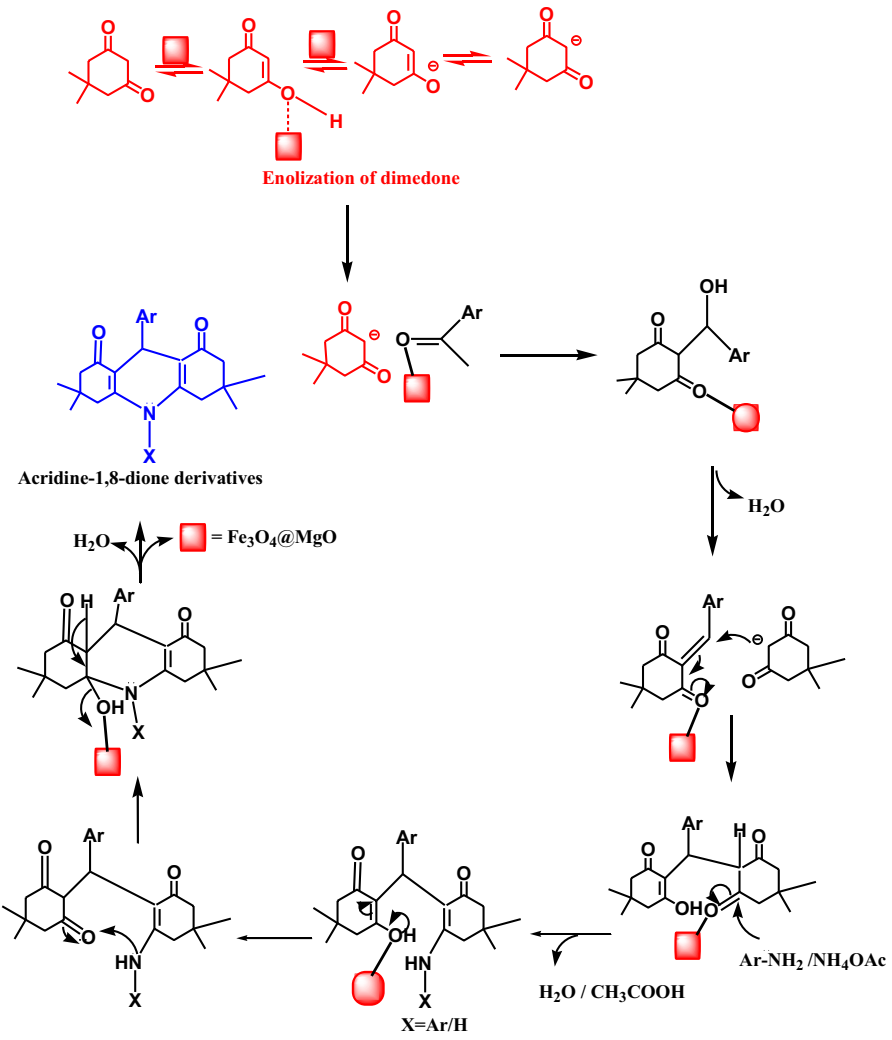


**Fig. 15** Plausible mechanism for synthesis of 3,3,6,6-tetramethyl-9-aryl-3,4,6,7,9,10-hexahydro-2H,5H-acridine-1,8-dione derivative by using $Fe_3O_4$@MgO catalyst

## Conclusion

The study aimed to develop a sustainable and efficient method for synthesizing derivatives of 3,3,6,6-tetramethyl-9-aryl-3,4,6,7,9,10-hexahydro-2H,5H-acridine-1,8-dione using $Fe_3O_4$@MgO core–shell nanoparticles as a catalyst. The nanoparticles have a core of $Fe_3O_4$ and a shell of MgO, which makes it easy to separate magnetically using an external magnet. The catalyst is environmentally friendly, can be easily recycled, and can be used for up to five consecutive cycles without any significant loss of catalytic activity. The reaction was carried out under ambient conditions,

**Table 5** Comparative study for the synthesis of 3,3,6,6-tetramethyl-9,10-diphenyl-3,4,6,7,9,10-hexahydro-2H,5H-acridine-1,8-dione derivative in the presence of previously reported catalyst[a] (Table 1, Entry 11)

| Sr. no | Catalyst | Catalyst loading | Solvent | Reaction conditions | Time (Min/Hr) | Yield[b] (%) | Ref no |
|---|---|---|---|---|---|---|---|
| 1 | Cu Doped ZnO | 5 mol% | Solvent-free | 90 °C | 1.5 Hr | 90 | [26] |
| 2 | Ag doped CdS | 10 mol% | $H_2O$ | ))))), RT | 15 | 81 | [64] |
| 3 | [Hmim]TFA | 0.1 g | Solvent-free | 80 °C | 4.5 Hr | 86 | [65] |
| 4 | FSG-Hf$(NPf_2)_4$ | 1 mol% | EtOH/$H_2O$ | Reflux | 6 h | 49 | [66] |
| 5 | MNP-[pmim]$HSO_4$ | 1 mol% | Solvent-free | 80 °C | 10 | 97 | [67] |
| 6 | CAN | 5 mol% | PEG 400 | 50 °C | 4 Hr | 96 | [68] |
| 7 | $Fe_3O_4$@Sap/Cu(II) | 0.42 mol% | $H_2O$ | RT | 05 | 96 | [69] |
| 8 | $Fe_3O_4$ NP's | 10 mol% | Solvent-free | 120 °C | 25 | 85 | [70] |
| 9 | $Fe_3O_4$@MgO | 15 mg | Solvent-free | 70 °C | 06 | 98 | Present work |

[a]Reaction conditions: benzaldehyde (1 mmol), dimedone (2 mmol), aniline (1 mmol);

[b]Yield of isolated product

**Table 6** Comparative study for the synthesis of 3,3,6,6-tetramethyl-9-phenyl-3,4,6,7,9,10-hexahydro-2H,5H-acridine-1,8-dione derivative in the presence of previously reported catalysts[a] (Table 1, Entry 1)

| Sr. no | Catalyst | Catalyst loading | Solvent | Reaction conditions | Time min | Yield[b] % | Ref no |
|---|---|---|---|---|---|---|---|
| 1 | B6 $(FC_5)_3$ | 3 mol% | Solvent-free | RT | 3.5 h | 80 | [71] |
| 2 | $TiO_2$ NP's | 10 mg | Solvent-free | 80 ºC | 20 | 90 | [29] |
| 3 | Silica-Supported Preyssler Nanoparticles | 0.03 mmol | $H_2O$ | Reflux | 2 h | 91 | [72] |
| 4 | $Fe^{3+}$/4A | 0.1 g | EtOH | Reflux | 14 h | 91 | [73] |
| 5 | $Fe_3O_4$@MgO | 15 mg | Solvent-free | 70 °C | 11 | 95 | Present work |

[a]Reaction conditions: benzaldehyde (1 mmol), dimedone (2 mmol), ammonium acetate (1 mmol)

[b]Yield of isolated product

where a range of aldehydes were converted to their respective acridine-1,8-dione derivatives with a yield of up to 98%. The methodology used was ecologically sound and solvent-free, making it an ideal alternative to traditional chemical methods. The reaction kinetics were fast, and the product output was substantial. Overall, this investigation showcases the use of a sustainable catalyst, which could potentially be used in other chemical reactions.

**Supplementary Information** The online version contains supplementary material available at https://doi.org/10.1007/s11164-023-05173-6.

**Acknowledgements** The authors acknowledge SAIF, IIT, Mumbai, SAIF, IIT, Madras, CSMCRI, Bhavnagar, DST-STIC, Cochin for extending instrumental support.

**Author contributions** Each author has contributed equally to the preparation and review of the manuscript.

**Availability of data** All pertinent information is presented within the manuscript and is available upon request from the corresponding author.

## Declarations

**Conflict of interest** The authors report no conflicts of interest. The authors alone are responsible for the content and writing of this article.

## References

1. A. Maleki, M. Panahzadeh, R. Eivazzadeh Keihan, Green Chem. Lett. Rev. **12**, 395 (2019)
2. O. Kamble, R. Chatterjee, R. Dandela, S. Shinde, Tetrahedron **120**, 132893 (2022)
3. D.K. Lang, R. Kaur, R. Arora, B. Saini, S. Arora, Anti-Cancer Agents Med. Chem. Anti-Cancer Agents **20**, 2150 (2020)
4. G. Grover, R. Nath, R. Bhatia, M.J. Akhtar, Bioorg. Med. Chem. **28**, 115585 (2020)
5. A. Mermer, T. Keles, Y. Sirin, Bioorg. Chem. **114**, 105076 (2021)

6. N. Sahiba, A. Sethiya, J. Soni, S. Agarwal, ChemistrySelect **6**, 2210 (2021)
7. O.I. El Sabbagh, H.M. Rady, Eur. J. Med. Chem. **44**, 3680 (2009)
8. A.A. Napoleon, F.R. Nawaz Khan, Med. Chem. Res. **23**, 4749 (2014)
9. A.S. Burange, K.G. Gadam, P.S. Tugaonkar, S.D. Thakur, R.K. Soni, R.R. Khan, M.S. Tai, C.S. Gopinath, Environ. Chem. Lett. **19**, 3283 (2021)
10. N. Kerru, L. Gummidi, S. Maddila, K.K. Gangu, S.B. Jonnalagadda, Molecules **25**, 1909 (2020)
11. A. Shokooh Saljooghi, H. Khabazzadeh, M. Khaleghi, J. Iran. Chem. Soc. **14**, 727 (2017)
12. P. Arora, V. Arora, H.S. Lamba, D. Wadhwa, Int. J. Pharm. Sci. Res. **3**, 2947 (2012)
13. M.M. Patel, M.D. Mali, S.K. Patel, Bioorg. Med. Chem. Lett. **20**, 6324 (2010)
14. K. Dzierzbicka, A.M. Kołodziejczyk, B. Wysocka-Skrzela, A. Myśliwski, D. Sosnowska, J. Med. Chem. **44**(22), 3606 (2001)
15. S. Sondhi, G. Bhattacharjee, R. Jameel, R. Shukla, R. Raghubir, O. Lozach, L. Meijer, Open Chem. **2**, 1 (2004)
16. F.W. Barros, T.G. Silva, M.G. da Rocha Pitta, D.P. Bezerra, L.V. Costa-Lotufo, M.O. de Moraes, M.O. Goulart, Bioorg. Med. Chem. **20**, 3533 (2012)
17. S.M. Sondhi, M. Johar, N. Singhal, S.G. Dastidar, R. Shukla, R. Raghubir, Monatshefte Für Chem. Chem. Mon. **131**, 511 (2000)
18. M. Kaya, Y. Yıldırır, G.Y. Çelik, Pharm. Chem. J. **48**, 722 (2015)
19. A. Davoodnia, A. Khojastehnezhad, N. Tavakoli-Hoseini, Bull. Korean Chem. Soc. **32**, 2243 (2011)
20. F. Moeinpour, A. Khojastehnezhad, J. Chem. **9**, 504 (2012)
21. B. Banerjee, G. Brahmachari, J. Chem. Res. **38**, 745 (2014)
22. M. Mokhtary, S.A. Mirfarjood Langroudi, Monatshefte Für Chem Chem. Mon. **145**, 1489 (2014)
23. A. Davoodnia, H. Norouzi, N. Tavakoli-Hoseini, A. Zare-Bidaki, Synth. React. Inorg. Met. Org. Nano Met. Chem. **44**, 70 (2014)
24. A. Nakhi, P.T.V.A. Srinivas, Md.S. Rahman, R. Kishore, G.P.K. Seerapu, K. Lalith Kumar, D. Haldar, M.V.B. Rao, M. Pal, Bioorg. Med. Chem. Lett. **23**, 1828 (2013)
25. S.M. Vahdat, H.R. Mardani, H. Golchoubian, M. Khavarpour, S. Baghery, Z. Roshankouhi, Comb. Chem. High Throughput Screen. **16**, 2 (2013)
26. H. Alinezhad, S. Mohseni Tavakkoli, Sci. World J. **2013**, e575636 (2013)
27. B. Maleki, R. Tayebee, M. Kermanian, S. Sedigh Ashrafi, J. Mex. Chem. Soc. **57**, 290 (2013)
28. K. Venkatesan, S.S. Pujari, K.V. Srinivasan, Synth. Commun. **39**, 228 (2008)
29. E. Eidi, M.Z. Kassaee, Z. Nasresfahani, Appl. Organomet. Chem. **29**, 793 (2015)
30. M.A. Zolfigol, N. Bahrami-Nejad, S. Baghery, J. Mol. Liq. **218**, 558 (2016)
31. N. Hasannezhad, N. Shadjou, J. Mol. Recognit. **35**, e2956 (2022)
32. C.W. Lim, I.S. Lee, Nano Today **5**, 412 (2010)
33. A. Maleki, R. Taheri-Ledari, R. Ghalavand, R. Firouzi-Haji, J. Phys. Chem. Solids **136**, 109200 (2020)
34. A. Maleki, R.F. Haji, M. Ghassemi, H. Ghafuri, J. Chem. Sci. **129**, 457 (2017)
35. A. Maleki, J. Rahimi, J. Porous Mater. **25**, 1789 (2018)
36. A. Maleki, H. Movahed, P. Ravaghi, T. Kari, RSC Adv. **6**, 98777 (2016)
37. Z. Hajizadeh, K. Valadi, R. Taheri-Ledari, A. Maleki, ChemistrySelect **5**, 2441 (2020)
38. A. Maleki, M. Kamalzare, Tetrahedron Lett. **55**, 6931 (2014)
39. A. Maleki, P. Ravaghi, M. Aghaei, H. Movahed, Res. Chem. Intermed. **43**, 5485 (2017)
40. H. Zou, Z. Luo, X. Yang, Q. Xie, Y. Zhou, J. Mater. Sci. **57**, 10912 (2022)
41. M.R. Ahghari, V. Soltaninejad, A. Maleki, Sci. Rep. **10**, 12627 (2020)
42. H. Atharifar, A. Keivanloo, B. Maleki, M. Baghayeri, H. Alinezhad, Res. Chem. Intermed. (2023)
43. F. Laffafchi, M. Tajbakhsh, Y. Sarrafi, B. Maleki, M. Ghani, Polycycl. Aromat. Compd. **43**, 3240 (2023)
44. M.B. Swami, G.R. Nagargoje, S.R. Mathapati, A.S. Bondge, A.H. Jadhav, S.P. Panchgalle, V. More, J. Appl. Organomet. Chem. **3**, 184 (2023)
45. B. Maleki, O. Reiser, E. Esmaeilnezhad, H.J. Choi, Polyhedron **162**, 129 (2019)
46. B. Li, R. Tayebee, E. Esmaeili, M.S. Namaghi, B. Maleki, RSC Adv. **10**, 40725 (2020)
47. H. Liu, M. Baghayeri, A. Amiri, F. Karimabadi, M. Nodehi, M. Fayazi, B. Maleki, E.N. Zare, A. Kaffash, Environ. Res. **231**, 116177 (2023)
48. B. Maleki, H. Atharifar, O. Reiser, R. Sabbaghzadeh, Polycycl. Aromat. Compd. **41**, 721 (2021)
49. M.B. Gawande, A. Goswami, T. Asefa, H. Guo, A.V. Biradar, D.L. Peng, R. Zboril, R.S. Varma, Chem. Soc. Rev. **44**, 7540 (2015)

50. L. De Matteis, L. Custardoy, R. Fernández-Pacheco, C. Magén, J.M. de la Fuente, C. Marquina, M.R. Ibarra, Chem. Mater. **24**, 451 (2012)
51. B. Kaboudin, F. Kazemi, F. Habibi, J. Iran. Chem. Soc. **12**, 469 (2015)
52. H. Peng, X. Wang, C. Hu, J. Hu, X. Tian, New J. Chem. **40**, 7911 (2016)
53. G. Shinde, J. Thakur, J. Chem. Sci. **135**, 14 (2023)
54. M. Ramezani Farani, M. Farsadrooh, I. Zare, A. Gholami, O. Akhavan, Catalysts **13**, 642 (2023)
55. J.P. Singh, V. Singh, A. Sharma, G. Pandey, K.H. Chae, S. Lee, Heliyon **6**, e04882 (2020)
56. S.A. Kulkarni, P.S. Sawadh, P.K. Palei, J. Korean Chem. Soc. **58**, 100 (2014)
57. L. Gan, Z. Lu, D. Cao, Z. Chen, Mater. Sci. Eng. C **82**, 41 (2018)
58. K.B. Ramesh, M.A. Pasha, Bioorg. Med. Chem. Lett. **24**, 3907 (2014)
59. S.R. Mousavi, H. Rashidi Nodeh, A. Foroumadi, Polycycl. Aromat. Compd. **41**, 746 (2021)
60. P. Mahesh, K. Guruswamy, B.S. Diwakar, B.R. Devi, Y.L.N. Murthy, P. Kollu, S.V.N. Pammi, Chem. Lett. **44**, 1386 (2015)
61. J.-J. Xia, K.-H. Zhang, Molecules **17**, 5339 (2012)
62. T.M. Hammad, J.K. Salem, R.G. Harrison, Superlatt. Microstruct. **47**, 335 (2010)
63. P. Samaddar, J. Hu, N. Barua, Y. Wang, T.A. Lee, M. Prodanović, Z. Heidari, T. Hutter, ACS Omega **7**, 43130 (2022)
64. D. Verma, V. Sharma, S. Jain, G.S. Okram, J. Dispers. Sci. Technol. **41**, 1145 (2019)
65. M. Dabiri, M. Baghbanzadeh, E. Arzroomchilar, Catal. Commun. **9**, 939 (2008)
66. M. Hong, G. Xiao, J. Fluor. Chem. **144**, 7 (2012)
67. H. Alinezhad, M. Tajbakhsh, N. Ghobadi, Res. Chem. Intermed. **41**, 9979 (2015)
68. M. Kidwai, D. Bhatnagar, Tetrahedron Lett. **51**, 2700 (2010)
69. M. Kazemnejadi, M.A. Nasseri, S. Sheikh, Z. Rezazadeh, S.A.A. Gol, RSC Adv. **11**, 15989 (2021)
70. M.A. Ghasemzadeh, J. Safaei-Ghomi, H. Molaei, Comptes Rendus Chim. **15**(11–12), 969–974 (2012)
71. S. Chandrasekhar, Y.S. Rao, L. Sreelakshmi, B. Mahipal, C.R. Reddy, Synthesis **2008**, 1737 (2008)
72. A. Javid, A. Khojastehnezhad, M. Heravi, F.F. Bamoharram, Synth. React. Inorg. Met. Org. Nano Met. Chem. **42**(1), 14–17 (2012)
73. Á. Magyar, Z. Hell, Catal. Lett. **149**, 2528 (2019)



## Authors and Affiliations

**Gayatree Shinde[1,2] · Jyotsna Thakur[2]**

✉ Jyotsna Thakur
thakurjyotsna@gmail.com

Gayatree Shinde
gayatree.g@gmail.com

[1] Smt. Chandibai Himathmal Mansukhani College of Arts, Science, Commerce and Management, Ulhasnagar 421003, India

[2] Changu Kana Thakur Arts, Commerce and Science College, New Panvel (W), Navi Mumbai 410206, India